Article

Harmonic nanoparticles: noncentrosymmetric metal oxides for nonlinear optics

ROGOV, Andrii, MUGNIER, Yannick, BONACINA, Luigi

Abstract

The combination of nonlinear optics and nanotechnology is an extremely rich scientific domain yet widely unexplored. We present here a review of recent optical investigations on noncentrosymmetric oxide nanoparticles with a large ${{\chi }^{(2)}}$ response, often referred to as harmonic nanoparticles (HNPs). HNPs feature a series of properties which distinguish them from other photonics nanoprobes (quantum dots, up-conversion nanoparticles, noble metal particles). HNPs emission is inherently nonlinear and based on the efficient generation of harmonics as opposed to fluorescence or surface plasmon scattering. In addition, the fully coherent signal emitted by HNPs together with their polarization sensitive response and absence of resonant interaction make them appealing for several applications ranging from multi-photon (infrared) microscopy and holography, to cell tracking and sensing

Reference

UNIVERSITÉ
DE GENÈVE

Topical Review

Harmonic nanoparticles: noncentrosymmetric metal oxides for nonlinear optics

Andrii Rogov[1], Yannick Mugnier[2] and Luigi Bonacina[1]

[1] GAP-Biophotonics, University of Geneva, Chemin du Pinchat 22, CH-1211 Geneva, Switzerland
[2] Univ. Savoie, SYMME, F-74000 Annecy, France

E-mail: luigi.bonacina@unige.ch

CrossMark

Abstract

The combination of nonlinear optics and nanotechnology is an extremely rich scientific domain yet widely unexplored. We present here a review of recent optical investigations on noncentrosymmetric oxide nanoparticles with a large $\chi^{(2)}$ response, often referred to as harmonic nanoparticles (HNPs). HNPs feature a series of properties which distinguish them from other photonics nanoprobes (quantum dots, up-conversion nanoparticles, noble metal particles). HNPs emission is inherently nonlinear and based on the efficient generation of harmonics as opposed to fluorescence or surface plasmon scattering. In addition, the fully coherent signal emitted by HNPs together with their polarization sensitive response and absence of resonant interaction make them appealing for several applications ranging from multi-photon (infrared) microscopy and holography, to cell tracking and sensing.

Keywords: multiphoton microscopy, second harmonic generation, third harmonic generation, nonlinear optics, nanophotonics, perovskites

(Some figures may appear in colour only in the online journal)

1. Introduction

Since the advent of ultrafast lasers in the early nineties and related availability of high peak power pulses at comparatively low energies, the investigation of nonlinear optical response have become a widespread activity resulting in innovative applications. In particular, in the field of imaging this has led to the introduction of multi-photon microscopy by W Webb [1]. This technique, as compared to one-photon excited fluorescence microscopy, features increased imaging depth, no out-of-focus bleaching, and spatial resolution comparable to confocal techniques without compromise in sensitivity. The latest technological advancements in this field are related to its extension towards longer wavelengths, facilitated by the timely introduction of novel tunable sources in the 0.7–1.3 μm spectral range and new optical components

with optimized performances in this region (microscope objectives, acousto-optic modulators, ...). Although these new infrared tunable devices are supposedly more adapted for imaging through thick (living) samples because of reduced scattering [2–4], the available choice of imaging targets (fluorescent molecules, dyes) with two-photon absorption bands >1200 nm is very limited.

Nanoparticle-based labelling, which is sometimes preferred over other approaches for its superior photo-stability, brightness, and chemical selectivity usually requires two-photon interactions in the 700–900 nm range, with a few notable exceptions [5]. However most optically active labels may suffer from bleaching and blinking and their use in biological research might be prevented because of low biocompatibility. For these reasons, since 2006, several research groups worldwide have proposed a complementary approach,

inherently nonlinear, based on the use of metal oxide non-centrosymmetric nanocrystals. Such particles lack an inversion symmetry centre in their crystal structure and therefore present an efficient $\chi^{(2)}$ response [6]. Their second harmonic (SH) emission can be used as optical contrast mechanism for imaging applications, so that they are often referred to as harmonic nanoparticles (HNPs). SH emission from HNPs features a series of appealing characteristics including orientation-dependent polarization patterns, coherent emission, and excitation wavelength tunability. This last property, which might seem counter-intuitive when thinking about frequency conversion in bulk phase-matched crystals, is directly stemming from the sub-coherence length dimensions of HNPs [7].

This review comes along the line of similar comprehensive works mostly devoted to the applications of HNPs as imaging probes for biological samples [8–10]. These previous contributions were explicitly intended for the nanotechnological community, while the purpose here is to review and disseminate the most recent results to the optics community to further stimulate interest for these photonics nanoprobes. The scope of this paper is limited to works published in the last decade on non-fluorescent, noncentrosymmetric, inorganic oxides with dimensions in the 20–200 nm range, purposely excluding investigations on the nonlinear optical response of semiconductor quantum dots and noble metal nanoparticles [11–15]. The following materials will be treated: $KNbO_3$, $BiFeO_3$ (BFO), $LiNbO_3$, $BaTiO_3$, $Fe(IO_3)_3$, $Ba(BO_2)_2$ (BBO), $KTiOPO_4$ (KTP), and ZnO. Notably, the first four entries are perovskites: beyond their nonlinear optical properties described here, such materials are under investigation for their piezoelectric and pyroelectric properties, and increasingly for their use in solar cell technology [16].

The review is structured in five sections. After a brief overview of the preparation of colloidal suspensions of HNPs based on different materials (section 2), we will address aspects related to signal intensity and stability over time and provide a quantitative comparison of SH efficiency for various materials (section 3). In the following section 4, the spectral properties of HNPs response will be reviewed both in terms of excitation and emission characteristics, with a paragraph dedicated to signals obtained by parametric nonlinearities other than SH. Successively, the polarization resolved response will be described along with a series of techniques developed in this framework in the recent past (section 5). Finally, several applications related to the coherent nature of the signal emitted by HNPs will be covered, including holography, phase-conjugation, and time-resolved schemes.

2. Synthesis and preparation of colloidal suspensions

The synthesis of noncentrosymmetric oxide nanoparticles has been addressed through varied chemical and physical routes, here we report just a few examples. $BaTiO_3$ and ZnO are commercially available since a few years (Nanostructured &

Amorphous Materials, Inc., Huston, TX). Usually both materials are produced by using either soft chemistry routes [17, 18] as well as hydrothermal conditions which have been proven to be quite efficient in the preparation of nanomaterials of desired size and morphology [19, 20].

For niobate materials, hydrothermal conditions were also used for preparation of $KNbO_3$ nanowires [20, 21] and solvothermal treatments for <50 nm $LiNbO_3$ HNPs [22]. In this latter case, shape control can be achieved by simply varying the initial amounts of reactants. Alternatively, $LiNbO_3$ can be synthesized by reduction of niobium salts and hydrolysis with LiH [23]. Other authors have proposed a molten salt approach using $KNbO_3$ as precursor [24]. Note also that colloidal suspensions of $KNbO_3$ HNPs have been recently commercialized (TiBio Sagl, Comano, Switzerland).

Nanometric KTP nanoparticles can be selected by centrifugation of raw powder remaining at the end of the flux-growth process leading to bulk KTP single crystal [25]. However, if a better control over crystalline quality and size dispersion is needed, co-precipitation can also be applied. This approach was originally reported by Biswas and coworkers [26] and recently further elaborated by Mayer *et al* [27, 28].

For the production of $Fe(IO_3)_3$, co-precipitation between iron nitrate and iodic acid has been used in homogeneous solutions and from mini [29]- and micro-emulsions [30, 31].

Finally BFO nanoparticles have been prepared by different methods including solvent evaporation [32], microwave hydrothermal conditions [33], combustion [34], and decomposition of glyoxylate precursor [35]. These works were mainly motivated by the specific multiferroics properties of bismuth ferrite. However, in terms of magnetic properties, the response of pure BFO is too weak [34] for being competitive with commonly employed magnetic nanoparticles (e.g. iron oxide NPs) in health-care applications [36].

After synthesis, colloidal dispersions are generally obtained by exposing the solution of HNPs to pulsed ultra-sonication. The solution pH depends on the stability region of the different materials, and it is fixed to 7 in most cases. Finally, a sedimentation period (up to one week) is necessary to eliminate larger aggregates. HNPs concentration at the end of the process can be estimated to be 10–30% of the initial one [37].

The approaches described are generally cost-effective and scalable (apart from microemulsions), leading to the synthesis of grams of product per batch. However, size dispersion of nanomaterials can be quite large as compared to other types of nanoparticles (see TEM images in figure 1) and the preparation of colloidal suspensions without aggregates requires careful and lengthy manipulation of the samples [37]. Some material syntheses seem to provide more homogeneous samples, e.g. $BaTiO_3$ [39, 40] and $LiNbO_3$ [22, 41]. For the successful translation of HNPs approach to relevant biomedical and commercial applications, a more controlled production is therefore highly sought for. This is even more so when considering that before the final use, HNPs should be further processed to increase their biocompatibility and target specificity [42–44].
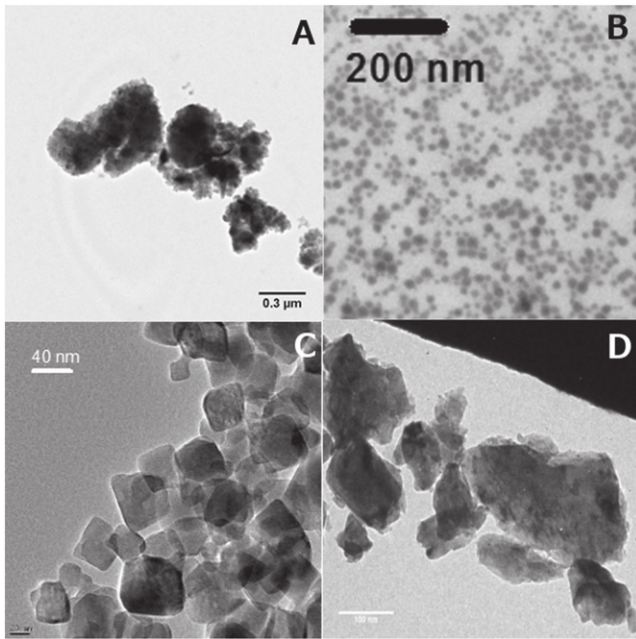
Figure 1. *HNPs transmission electron microscopy images.* (A) Agglomerates of commercial ZnO nanocrystals with a mean size 45 nm. Reprinted with permission from [38]. Copyright 2011 American Chemical Society. (B) Spherical nanocrystals of $Fe(IO_3)_3$ obtained by PEG-modified microemulsion route. Reprinted with permission from [31]. Copyright 2012 American Chemical Society. (C) Cubic $LiNbO_3$ nanocrystals produced by hydrothermal synthesis. (D) BFO nanoparticles synthesized by combustion. Reprinted with permission from [34]. Copyright 2011 AIP Publishing LLC.

3. Signal intensity and photo-stability

Brightness, photostability, and contrast against background are the physical properties which are crucial for the choice of a nanoprobe. For bio-oriented applications, of course these characteristics should be complemented by the NPs biochemical behaviour in terms of targeting efficiency and biocompatibility, which are out of the scope of the present review and have been treated elsewhere [9].

3.1. Signal intensity

Because the optical response of HNPs is inherently nonlinear, when comparing their signal generation efficiency with that of other nanoprobes, one has first to consider that higher power density is required by the nonlinear interaction as compared to linear one. Therefore, in terms of bare conversion efficiency of incoming photons into emitted signal photons, linear probes like quantum dots are more attractive. Once other criteria come into play (excitation tunability, photo-stability, imaging depth in scattering samples, coherence, contrast against background) the choice for harmonic probes might become relevant. As the harmonic response of HNPs is not a surface effect (at least for sizes >20−30 nm) [41, 45], individual particles volume V plays a major role, as the SH signal scales as V^2.

A first rough efficiency comparison in the literature was provided by Hsieh *et al* in 2009 for individual 90 nm $BaTiO_3$

HNPs. The authors compared the value obtained (400–4800 GM)[3] with the two-photon excited fluorescence efficiency of typical fluorescent molecules (75 GM for enhanced green fluorescent protein) and CdSe quantum dots (47000 GM) [42, 46]. Although useful as a general guideline, the validity of this comparison is limited by several factors, including (i) the exact determination of the HNP size and orientation with respect to the laser polarization (see section 5), and (ii) the difficulty to quantitatively retrieve the total number of emitted photons. This second aspect is related to the interplay between the limited N.A. of the microscope objective and the non-isotropic nonlinear emission from nanometric objects which presents a pronounced size dependence [47]. For these reasons, optical measurements on particle ensembles independently characterized in terms of size and size-distribution, can be helpful for setting the accuracy of the measurements in a more robust statistical fashion.

3.2. Averaged SH coefficient by hyper Rayleigh scattering

Hyper-Rayleigh scattering is an ensemble technique originally developed for determining the second order hyperpolarizability $\langle \beta \rangle$ of molecules in solution averaged over all possible orientations [48, 49]. The technique can be adapted to measure nanocrystals' response under certain approximations (HNP size not exceeding 100 nm, introduction of an effective local field factor) [38, 50]. This way, provided a preliminary calibration with a substance with known response, the average second order nonlinear efficiency can be estimated as $\langle \beta \rangle = \langle d \rangle V$, where $\langle d \rangle$ is the averaged SH coefficient, and V is the HNPs volume. V is to be independently determined, typically by TEM imaging, dynamic light scattering or nanoparticles tracking analysis [51].

The $\langle d \rangle$ values for several HNPs nanomaterials are reported in table 1, together with the corresponding crystal symmetry point group. These quantities were obtained from HRS measurements by using the external reference method with paranitroaniline (pNA) molecules diluted in methanol. The macroscopic averaged nonlinear coefficient $\langle d \rangle$ was derived from the pNA molecular hyperpolarizability ($\langle \beta_{pNA} \rangle = \sqrt{\frac{6}{35}} \beta_{33}$ with $\beta_{33} = 25.9 \times 10^{-30}$ esu expressed here in the convention 1 as defined in the reference book by Kuzyk and Dirk [52]. The relationship between the molecular hyperpolarizability β and the macroscopic nonlinear coefficient d can be written as $d = \chi^{(2)} = N f_\omega^2 f_{2\omega} \beta$, where N is the number density of formula units in the crystal and f_ω and $f_{2\omega}$ are the local field factors at the fundamental and SH frequency, respectively [38, 50].

In general, the $\langle d \rangle$ values obtained by HRS for nanocrystals are comparable to those reported for bulk materials [37, 38, 50]. The exact expression to relate $\langle d \rangle$ to the d_{ij} tensor coefficients depends on the specific crystal symmetry [50]. One can see how BFO presents by far the strongest efficiency among the materials under scrutiny.

---

[3] Göppert-Mayer unit—1 GM = 10^{-50} cm^4 s photon^{-1}.

Table 1. HNPs symmetry properties and average second harmonic coefficient $\langle d \rangle$.

HNP material	Point group	$\langle d \rangle$ by HRS (pm V^{-1})	d tensor (Kleinman symmetry)
LiNbO$_3$	3m	5−7	$\begin{pmatrix} 0 & 0 & 0 & 0 & d_{15} & -d_{22} \\ -d_{22} & d_{22} & 0 & d_{15} & 0 & 0 \\ d_{15} & d_{15} & d_{33} & 0 & 0 & 0 \end{pmatrix}$
BiFeO$_3$		60−80	
KNbO$_3$	mm$_2$	5−8	$\begin{pmatrix} 0 & 0 & 0 & 0 & d_{15} & 0 \\ 0 & 0 & 0 & d_{24} & 0 & 0 \\ d_{15} & d_{24} & d_{33} & 0 & 0 & 0 \end{pmatrix}$
KTP		1−3	
BaTiO$_3$	4 mm	5−6	$\begin{pmatrix} 0 & 0 & 0 & 0 & d_{15} & 0 \\ 0 & 0 & 0 & d_{15} & 0 & 0 \\ d_{15} & d_{15} & d_{33} & 0 & 0 & 0 \end{pmatrix}$
ZnO	6 mm	1−3	
Fe(IO$_3$)$_3$	6	5−7	$\begin{pmatrix} 0 & 0 & 0 & 0 & d_{15} & 0 \\ 0 & 0 & 0 & d_{15} & 0 & 0 \\ d_{15} & d_{15} & d_{33} & 0 & 0 & 0 \end{pmatrix}$

Interestingly, Grange *et al* have observed a distortion from the bulk-like behaviour for BaTiO$_3$ HNPs < 30 nm, and evoked competing effects like surface contribution and deviation from the crystalline structure of the nanomaterial in this size range. This explanation is also supported by polarization resolved emission measurements (see also section 5) which do not display the expected symmetry for the BaTiO$_3$ point group 4 mm [45]. On the other hand, Knabe *et al* did not observe any size effect in the 5–50 nm diameter range for LiNbO$_3$ nanocrystals [41].

3.3. Photo-stability

Several authors have demonstrated the absence of bleaching, quenching, and blinking in HNPs response [24, 25, 37] and highlighted the benefits for imaging in terms of signal-to-noise ratio and long-term monitoring of evolving structures [53, 54]. Indeed most mechanisms of signal intensity decay and/or variations over time are related to the excitation of resonant electronic states. Cumulative single and multi-photon absorption/emission cycles in quantum dots, up-conversion NPs, and dye-loaded NPs may result into permanent modifications of optical properties by heating and ionization. Trapping state at the surface of quantum dots or internal conversion in fluorescent molecules leading to spin forbidden transitions, also affect the stability of the optical response over time. Such mechanisms are not present in HNPs, as laser excitations in the visible and infrared region are non-resonant with transitions to any real state of the system. The striking difference between the HNPs behaviour and that of a cell-membrane fluorescent dye can be appreciated in the comparison reported in figure 2, where the fluorescence signal is completely vanished after a 10 min long raster-scan whereas the SH intensity from the HNPs has remained constant. Notwithstanding these considerations, some authors have observed that when using a non-scanning excitation and focusing over extended time on a specific HNP, some optical modifications might take place. Such effects are likely to be
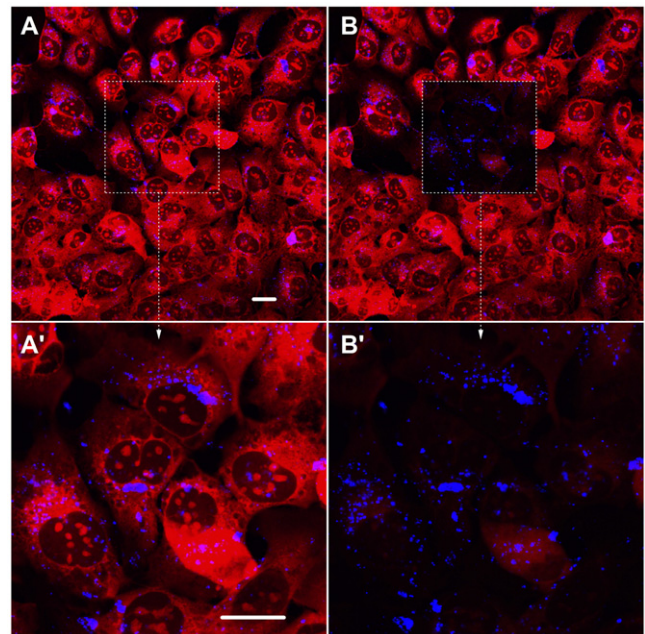
Figure 2. *Signal photostability.* Multiphoton imaging of bronchial epithelial cells exposed for 5 h to PEG-coated KNbO$_3$ HNPs, imaged before (A), (A$'$) and after (B), (B$'$) a 10 min long raster scan limited to the area of the dashed rectangle. Two-photon excited fluorescence of cell membrane is in red; SH from HNPs in blue. Scale bars: 20 μm.

induced by the heating of the volume surrounding the HNPs. For example, Li *et al* have observed permanent modifications of the response of a single BaTiO$_3$ HNP attached via a carbon nanotube to a nanowire [55]. Backed up by control experiments, the authors have ascribed this change to the transition of BaTiO$_3$ nanocrystals from tetragonal to cubic phase due to the heating of the neighbouring carbon nanotubes. In another experiment requiring extended irradiation (hours) of a individual HNP without scanning, Extermann *et al* increased the long term signal stability blocking the laser for short periods

(seconds) to let the excessive heat evacuate from the focal volume [56].

3.4. Plasmonic enhancement of SH efficiency

In 2010 Pu *et al* demonstrated a promising application of plasmonic enhancement based on $BaTiO_3$ HNPs surrounded by a nanometric gold shell [57]. Differently from other well-investigated metal core—metal shell plasmonic structures [11], where even order nonlinear signal (e.g. SH) are generated because of the symmetry breaking at the interfaces, in this case, the whole core volume participates to the generation of the nonlinear signal. The enhancement factor corresponds to $\Gamma_{2\omega} = [\frac{E_{c-shell}}{E_c}]^4 T_{2\omega}$, where $T_{2\omega}$ is the shell transmission at the SH frequency, while $E_{c-shell}$ and E_c are the fields in the noncentrosymmetric core with and without the metal shell, respectively. The authors calculated by exact Mie theory a 3500-fold enhancement factor at resonance (700 nm) and were able to show experimentally a factor 500. The Grange group, in a successive publication, could show the presence of resonance peaks by tuning the excitation wavelength in Au-coated $KNbO_3$ nanowires. In this work the structure was designed to shift the resonance to 900 nm, with clear advantages for imaging penetration depth [58]. More recently, the same team has addressed the issue of coating homogeneity by comparing the output of two different preparations based respectively on aminosilane and polyelectrolyte film coating, suggesting that the second method is preferable [59]. The enhancement factor measured at 900 nm is 250.

Although the HNP-core/metal-shell approach is sound from the theoretical point of view, its technical realization is severely affected by issues related to reproducibility and sample homogeneity: size and shape control of the inorganic core and the shell thickness are mandatory to obtain a significant enhancement, at a given wavelength, for an ensemble of plasmonic nanostructures. Moreover, it might be difficult to shift the resonance above >1.1 μm to take full advantage of the new generation of ultrafast laser sources.

4. Spectral properties

4.1. Excitation wavelength tunability

A rather interesting property of HNPs is their minimal sensitivity to the excitation wavelength. Contrary to their bulk nonlinear counterparts, no phase-matching constrain applies, as the nanocrystals are much smaller than the material coherence length. In other words, no destructive interference is taking place between the signals emitted at different locations within the particles. Figure 3 shows the experimental SH spectra obtained using different femtosecond laser sources (erbium ion [3], chrome forsterite [61], tunable Ti:sapphire [37], frequency doubled Ti:sapphire [60]) on individual HNPs. One can see how the spectral range from the deep ultraviolet to the near infrared is covered. This possibility represents a great advantage with respect to other nano-technology approaches based on resonant excitation and with
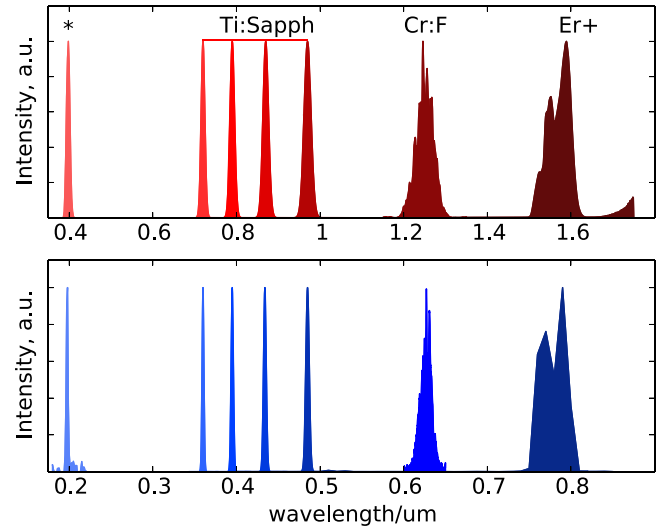

Figure 3. *Excitation wavelength flexibility*. Upper panel: experimental laser spectra (Er+: erbium ion, Cr:F: chromium-activated forsterite, Ti:sapph:titanium sapphire, *:frequency doubled Ti: sapphire). Lower panel: corresponding SH emission from individual HNPs [3, 37, 60, 61].

fixed spectral properties. In particular, longer wavelengths are less prone to scattering and allow deeper imaging in thick samples [3]. On the other hand, the generation of narrow bandwidth spectra through the ultraviolet and visible region can be used to exert selective interaction with the HNPs surrounding, for example to trigger a specific molecular response [62].

It should be however mentioned that some authors have reported a certain spectral dependence in terms of nonlinear conversion efficiency. Pantazis *et al* compared the SH efficiency of ZnO, $BaTiO_3$, and SiC in the 760–970 nm and found that it decreases for increasing excitation wavelength, in a more pronounced way for ZnO and SiC than for $BaTiO_3$. They have ascribed this finding to the spectral position of the bandgap, which—for some materials—is close to resonance (at 2ω) at the shortest excitation wavelengths [63].

4.2. Frequency mixing and higher harmonics generation

Although SH generation is the most investigated among second order nonlinear processes, sum and difference frequency generation are equally expected from HNPs given their large $\chi^{(2)}$ values. In 2007 Nakayama *et al* reported for the first time the simultaneous sum frequency and harmonic generation in $KNbO_3$ nanoneedles [21]. The Prasad group successively showed that ZnO nanocrystals can efficiently mix 1064 and 850 nm light to generate 472 nm [64]. Interestingly, they also observed a $\chi^{(3)}$ process: $2\omega_1 - \omega_2$ four wave-mixing leading to 708 nm emission. Later, sum frequency generation obtained by mixing the extreme blue and red frequency tails of an ultrabroadband (100 nm at FWHM) femtosecond pulse was demonstrated by Wnuk and co-workers [65]. At present, difference frequency generation and optical rectification have not been reported, likely because of the difficulty of transmitting/detecting mid-IR wavelengths in

a microscope set-up and, in the case of THz generation via optical rectification, because of issues related to far field propagation of such long wavelengths generated by nano-metric sources.

Extermann *et al* firstly reported the simultaneous gen-eration of SH and third harmonic (TH) in $Fe(IO_3)_3$ NPs excited at 1.55 μm. The measured SH/TH ratio was approximately 100 [3]. The presence of strong higher order nonlinear response in large $\chi^{(2)}$ materials is not surprising, Morita and Yamashita proposed an analytic expression relating the magnitude of $\chi^{(2)}$ and $\chi^{(3)}$ for the nonresonant region of noncentrosymmetric materials with $\chi^{(2)} \geqslant 10$ pm V^{-1}, therefore in the range of HNPs response. Under these assumptions they demonstrated that $|\chi^{(3)}| \propto |\chi^{(2)}|^2$ [66]. However, reports on higher harmonics generated by HNPs are still very sparse, principally due to the fact that wavelengths <350 nm are not transmitted by standard microscope objec-tives, while the TH of tunable Ti:sapphire laser (by far the most common among multiphoton sources) is <330 nm.

Cai *et al* have recently investigated the generation of SH and TH in $KNbO_3$ needles with relative large dimensions (length exceeding 1 μm) [67]. The authors do not report the intensity ratio among $\chi^{(2)}$ and $\chi^{(3)}$ responses, but they provide an interesting study on their spectral dependence showing the presence of relative maxima that might be correlated with the electronic properties of the materials, similarly to what was suggested by Pantazis for SH [63]. Dai *et al* have published a quantitative study on the competing effect of the two har-monics using excitation wavelengths spanning from 1150 to 1350 nm, based also in this case on relative large particles (ZnO rods, 250 nm diameter for 2 μm length) [68]. The authors have shown that by modifying the excitation intensity from 0.05 to 1.2 TW cm^{-2} the SH/TH ratio can be reduced even to values <1, owning to the different intensity depen-dence of the two harmonic orders. The authors suggest that this result can be exploited for display applications.

Geissbuehler *et al* reported the simultaneous detection of SH and TH from $KNbO_3$ HNPs in calf serum using a flowing correlation spectroscopy set-up pumped by a chromium-activated forsterite laser at 1250 nm [61]. This study indicates that the cross-correlation among these spectrally separated harmonic signals can effectively increase HNP detection selectivity in presence of optical interferents in a complex medium. The same approach based on simultaneous detection of multi-order harmonics for increased selectivity against endogenous background (i.e. collagen for SH and lipids for TH) [69] has now been demonstrated for imaging at 1.25 μm [70].

In parallel to investigations involving parametric non-linear techniques, a hybrid HNP-upconversion approach has been proposed for diversifying the spectral emission by synthesizing core-shell heterostructures consisting of a KTP core and a $LaPO_4$:Eu matrix shell. These particles exhibit both SH and a rich photoluminescence emission spectrum throughout the visible region [28].

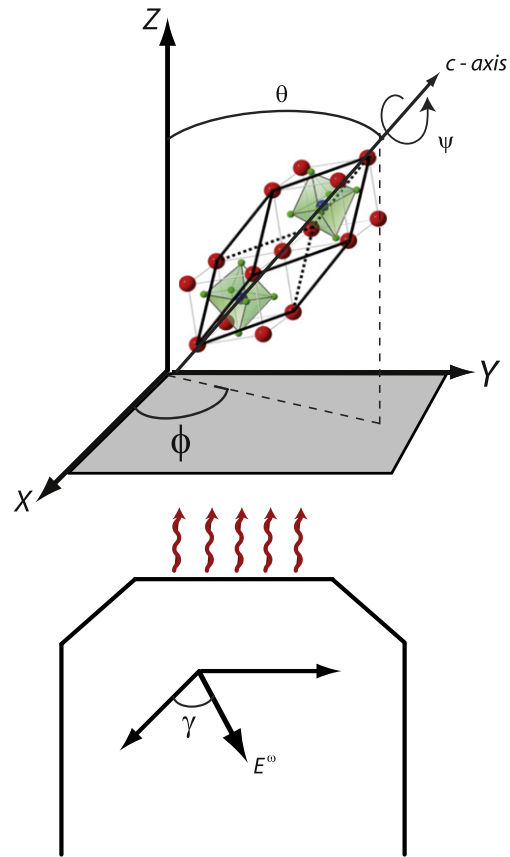**Figure 4.** *Polarization microscopy.* The crystal orientation is expressed in the laboratory frame X, Y, Z by the Euler angles ϕ, θ, and ψ. The angle γ denotes the polarization of the incident laser light on the sample plane.

5. Polarization properties

As previously mentioned and differently from other approa-ches, SH generation by HNPs is a bulk phenomenon invol-ving the whole particle volume rather than a surface one. The emission efficiency is therefore modulated by the orientation of the particle lattice with respect to the laser polarization. A theoretical framework for dealing with the polarization response of noncentrosymmetric particles in the focus of a high N.A. objective was developed in 2003 by the Zyss group [7, 71].

The components of the nonlinear polarization vector $P^{(2)}$ are related to the crystal second order susceptibility tensor by $P_i^{(2)} = \epsilon_0 \sum_{jk} \chi_{ijk}^{(2)} E_j^\omega E_k^\omega$, where $E_{i=x,y,z}^\omega$ are the components of the incident field at the fundamental frequency ω. The crystal nonlinear susceptibility tensor, $\chi_{ijk}^{(2)}$, is expressed here in the laboratory frame. Using an appropriate rotation operator $\hat{S}$, this tensor can be expressed in the crystal reference frame: $\chi_{ijk}^{(2)} = \sum_{\bar{i}\bar{j}\bar{k}} \chi_{\bar{i}\bar{j}\bar{k}}^{(2)} S_{i\bar{i}} S_{j\bar{j}} S_{k\bar{k}}$, where $S_{i\bar{i}}$ are the components of the rotation matrix between the laboratory and crystal axes depending on the Euler angles ϕ, θ and ψ, defined according to the scheme in figure 4.

A straightforward application of this model is the deter-mination of individual nanocrystals orientation. From the
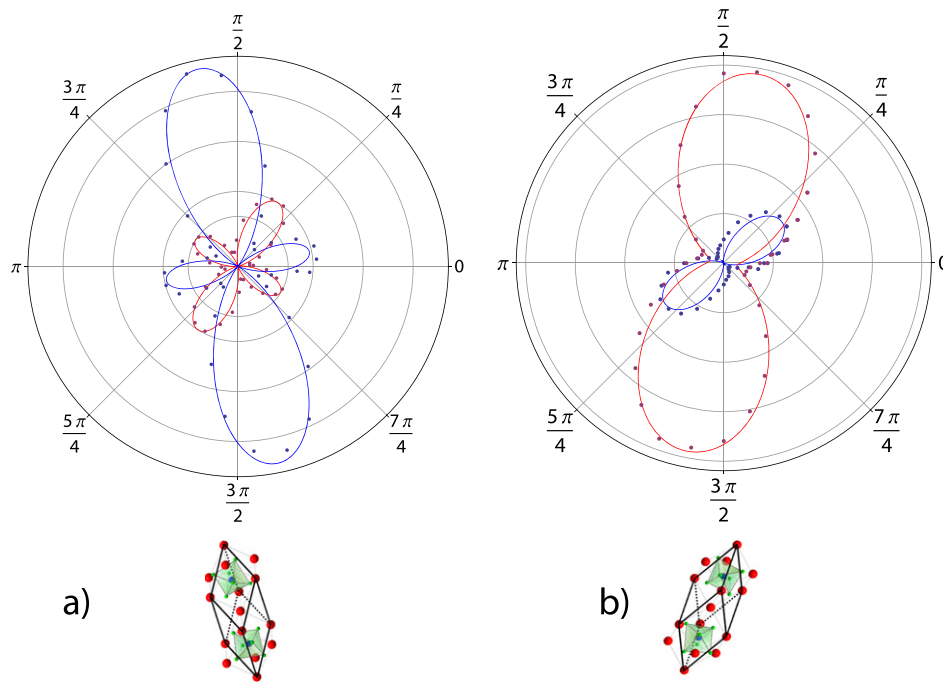
Figure 5. *Polarization-resolved emission of BFO HNPs.* Each signal is analysed along two orthogonal directions: *X* (blue trace) and *Y* (red trace). Dots correspond to experimental data, while solid lines represent the best fit, yielding the following values for Euler angles: (a) $\theta = 150°$, $\phi = 281°$, $\psi = 275°$, (b) $\theta = 141°$, $\phi = 69°$, $\psi = 330°$.

experimental standpoint, the SH intensity is collected as a function of the in-plane polarization angle of incident light, γ, for two orthogonal positions of an analyser set in front of the detector. Examples of angular resolved SH traces acquired by applying this procedure on two different individual BFO HNPs are shown in figure 5. In these polar plots, symbols correspond to the measured datapoints, lines to the fit obtained by fixing the $\chi^{(2)}$ tensor and letting the three Euler angles vary as free parameters. This approach has been used by several authors, both for orientation retrieval or vice versa for determination of $\chi^{(2)}$ tensor elements for a given crystal symmetry. Specifically, in the literature, one can find polarization resolved emission traces for $Fe(IO_3)_3$ [72], BBO [73] KTP [27, 28, 74], $LiNbO_3$ [41, 75], $BaTiO_3$ [38, 76], ZnO [38], BFO [34]. One remarkable observation, mutual to several of these studies, is that the bulk tensorial elements $\chi^{(2)}_{ijk}$ can be safely applied to describe the response of these nanoobjects [37, 41], even though for materials less characterized in their macroscopic form some discrepancies are present in the literature [34]. These differences should be in part (but not exclusively) ascribed to different protocols for material synthesis and crystalline purity.

For correctly interpreting polarization plots as the ones in figure 5, several distortions from the polarization response of microscope optics (including dichroism, ellipticity, distortion induced by high N.A. objective) should be taken into account and corrected for. The Brasselet group provided a very useful and detailed description in this sense, proposing an effective calibration procedure of the polarization response of a microscope set-up [77]. The Psaltis group has studied the difference in emission when circular polarization is used

instead of linear one for excitation [76], and reported that the nonlinear response under circularly polarized excitation is generally inferior in intensity to the average of linear excitations over all orientations.

As some authors have pointed out, the polarization fitting procedure for orientation retrieval, is particularly effective for determining the in-plane angle ϕ. However for more complex symmetry point groups, there might exist an interplay between the off-plane angle θ and the SH signal intensity, which is on its turn strongly modulated by the particle dimensions. Therefore, without an *a priori* knowledge of particle size it might be difficult to retrieve the three-dimensional orientation with a high degree of certainty. The group of Brasselet originally proposed to combine the anisotropic polarization response of SH with that of two-photon excited fluorescence to increase the number of observables used for the fitting procedure. Unfortunately, this more robust approach is not applicable in the case of non-fluorescent HNPs [7].

Recently, a general methodology for investigating the symmetry of *unknown* SH active objects has been proposed [78] and experimentally validated by van der Veen *et al* [79] This approach allows the *in situ* determination of the point group symmetry of unknown noncentrosymmetric structures. The analysis is based on a series of binary tests based on observables such as the presence of SH emission and symmetry of the polarization plot under specific settings for analyser and polarized excitation. Other algorithms for the fast retrieval of the symmetry have also been proposed [80]. The Rabitz group has theoretically investigated the possibility of using phase-shaped ultrafast laser pulses for acting
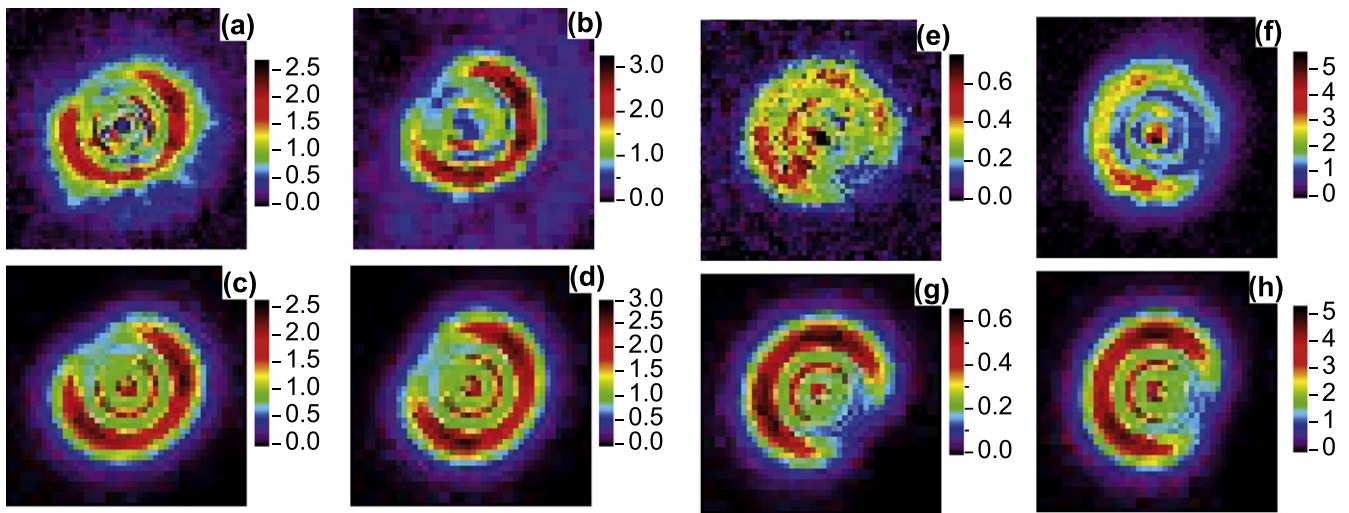
Figure 6. *Orientation retrieval by defocused imaging.* (a)–(d) and (e)–(h) examples of defocused images of two single KTP nanocrystals. Experimental (top) and calculated (bottom) images are obtained for different incident polarization directions relative to the *X* axis: 0° (a), (c), (e), (g) and 90° (b), (d), (f), (h). The nanocrystals are found to be oriented along the $[\theta = 67°, \phi = 46°, \psi = 45°]$ direction (left) and $[\theta = 55°, \phi = 65°, \psi = 90°]$ direction (right). Reprinted with permission from [74]. Copyright 2007 The Optical Society.

independently on SH and sum frequency generation, exploiting the sensitivity of these two observables on crystal axis orientation and pulse duration. As a conclusion of the study, the authors did not find any coupling among time-profile and polarization [81].

5.1. Defocused imaging

A flaw of the polarization resolved measuring procedure just described is related to the rather lengthy measuring time necessary to acquire a full polarization plot like the ones in figure 5. Even when both detection polarization are acquired simultaneously (with a polarization splitting cube) the excitation polarization should be sequentially incremented over sufficiently small rotation steps by a $\lambda/2$ plate. To address this issue, first Sandeau *et al* [74] and successively Baumner *et al* [82] have applied defocused imaging analysis to retrieve the HNP in-plane polarization in a single measurement. The technique, adapted from the field of single molecule imaging, relies on acquiring out-of-focus SH images of individual HNPs placed at the focus of an infinitely-corrected objective. The detector (usually a CCD camera) is located on a plane away from the focus image point of the imaging lens [83–85]. As one can see from figure 6, the defocused patterns feature a symmetry axis along the projected direction of the nonlinear induced dipole $P^{(2)}$ (angle ϕ in figure 4). The concentric ring-structure can be related (supported by a vectorial calculation) to the tilt angle of crystal unit cells with respect to the optical axis (angle θ in figure 4) [74]. As correctly pointed out by Sandeau *et al*, the modelling is limited to nanoparticles in the Rayleigh regime, with diameter $<100-150$ nm.

5.2. Applications of polarization-sensitive response

Following the results of a seminal paper by Brasselet *et al* [71], the crystal orientation sensitivity of SH HNPs emission

has been mostly used for *in situ* diagnostics of nanoobject crystal purity. In fact, provided that the $\chi^{(2)}$ tensor of the HNPs sample is known, it is straightforward to associate polar plots which do not fit with the solutions associated with a specific lattice structure with polycrystalline aggregates [72, 74]. Grange, has used polarization resolved imaging to monitor the rotation of a LiNbO$_3$ nanowire electrically manipulated in a fluidic set-up [75]. A similar approach has been followed by the Roch group to monitor the orientation of KTP HNPs in *in vitro* cortical neurons cultures, with prospective applications for monitoring charge transients in cells cultures [27]. Very recently, SH intensities variations of HNPs have been used to study translational and rotational diffusion of particles uptaken by living cells [54]. This measurement is based on wide field detection for maintaining extremely short image acquisition times (50 μs). Therefore, differently from scanning microscope techniques, it requires a KHz amplified laser system instead of a MHz oscillator.

6. Exploiting signal coherence

One of the most prominent features of HNPs which to the authors' opinion is still largely unexploited is their fully coherent optical response, which can be appreciated by inspecting the interference pattern generated by two neighbouring nanoparticles, shown in figure 7(a). In this example, the emission is excited by an evanescent wave propagating along a waveguide [82]. Note that such coherent patterns among emissions of nano-objects cannot being formed if images are acquired in a raster scanning fashion. This measurement can be considered as a nonlinear analogue of Young's double slit experiment, where the particles act as point sources emitting the SH of the evanescent wave frequency and interfere in the far-field. The accompanying simulation in figure 7(b) is obtained within the framework
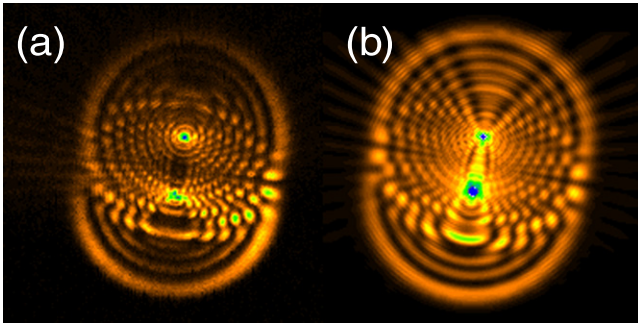
Figure 7. *Coherent optical response.* Experimental (a) and numerical (b) defocused images of two adjacent nanoparticles excited by an evanescent field and interfering at the SH frequency. Reprinted (adapted) with permission from [82]. Copyright 2010 The Optical Society.

developed for defocusing imaging of single molecules, as introduced in section 5 [84].

6.1. Ultrashort pulses characterization

A first phase-sensitive approach, which can be extremely useful for characterizing a femtosecond pulse at the focal plane of a high N.A. objective with sub-diffraction limited resolution was presented by Extermann *et al* [56]. In that case, an interferometric set-up was used to delay in time two replicas of a beam collinearly focused by a 1.3 N.A. 110× objective onto a HNP. The signal generated by the particle in the focus was epi-collected and spectrally resolved. By varying the time delay a collinear frequency resolved optical gating (FROG) trace was acquired. The high frequency components appearing due to the parallel beam geometry can be eliminated by Fourier filtering [86] and the resulting non-interferometric FROG spectrogram can be inverted by established algorithms to retrieve information about the spectral phase of the pulse at the focus [87]. A similar approach was successively applied in a series of experiments by the Liu group, attaching a HNP on a fiber taper via a carbon nanotube [88, 89] making it possible to manipulate the probe with high precision via a piezoelectric stage for acquiring autocorrelation traces at the laser focus, using the HNP as nonlinear medium. The same device was successively used to detect a holographic FROG trace probing the evolution of a pulse at different locations in space [90].

The quadratic sensitivity of the SH response on the excitation pulse peak power has been evidenced by several authors. Interestingly Wnuk *et al* have shown how a decrease of pulse duration at the sample can greatly benefit the image contrast and sensitivity (figure 8), demonstrating that the signal-to-noise ratio of isolated KTP HNPs can be seven-fold improved when the pulse duration is decreased from 200 to 13 fs keeping all other parameters constant [65]. Conversely, thanks to their photo-stability and the absence of saturation, HNPs are increasingly employed as local probes to effectively pre-compensate the dispersion accumulated by a femtosecond pulse propagating through microscope optics (objectives can induce second order dispersion of the order of 10^3 fs^2) [91].

Interestingly, higher dispersion orders, which cannot be corrected for using grating or prism compressors, can be acted upon by the use of a pulse shaper. In this case, a phase-mask is applied to the pulse spectrum spatially dispersed in the Fourier plane of a 4*f* compressor and the spectral phase is optimized in a close-loop fashion using as a feedback the SH of a HNP placed at the objective focus [65]. Recently, Accanto *et al* [92] have explored this approach and used the multiphoton intrapulse interference phase scan technique for pulse temporal compression [93]. In the same work, they demonstrated intra-pulse interferences, by setting a π phase step at the spectral maximum ω of the exciting pulse to modulate the spectral intensity at 2ω.

6.2. Coherent technique for increasing sensitivity

In 2006, Le Xuan *et al* demonstrated the coherent optical homodyne detection of the nonlinear signal from a single isolated KTP nanocrystal [94]. In their experimental arrangement, the signal field is represented by the emission at 2ω, $E_{\text{HNP}}^{2\omega}$, which is epi-collected by the objective. The local oscillator used for homodyne detection is generated outside the microscope by sending part of the fundamental infrared beam into a bulk crystal for frequency doubling. The actual detection is assured by a pair of two balanced avalanche photodiodes, used respectively at ω and 2ω. By processing the interferences acquired simultaneously at the two frequencies, the authors could extract the relative phase $\Phi_{\text{HNP}}^{2\omega}$ of the particle, where $E_{\text{HNP}}^{2\omega} = |E_{\text{HNP}}^{2\omega}| \exp(\text{i}\Phi_{\text{HNP}}^{2\omega})$. Such phase term is associated with the projection on the focal plane of the nonlinear polarization vector, and yields information about the HNP orientation.

6.3. Holography and phase-conjugation

In 2008, the Psaltis group demonstrated the possibility of holographic recording of the nonlinear emissions of HNPs [95]. As this approach relies on illuminating a rather large sample area, an amplified Ti:sapphire system is required to assure the necessary light intensity (10^{11} W cm^2). In the experiment, the SH emission of rather large BaTiO$_3$ clusters ($\sim$10 μm) was superimposed on a 2ω reference beam separately generated in a bulk frequency doubling crystal. The spatially resolved interference pattern was acquired by a highly sensitive two-dimensional detector (EM-CCD). The interferences recorded this way convey information on the axial position of the different emitters. Shortly after, the approach was extended to imaging HeLa cells labelled by nanometric BaTiO$_3$ nanocrystals [42]. The advantage of this technique is clearly related with its speed, as relatively large volumes can be imaged in three dimensions in a non-scanning fashion.

Successively, harmonic holography was coupled to phase conjugation to perform coherent images through highly scattering media. In this case, HNPs assume the role of point-sources necessary to define the phase-conjugated wavefront at 2ω to counteract scattering. In the experimental realization, a coherent beam at ω is focused through a scattering layer of
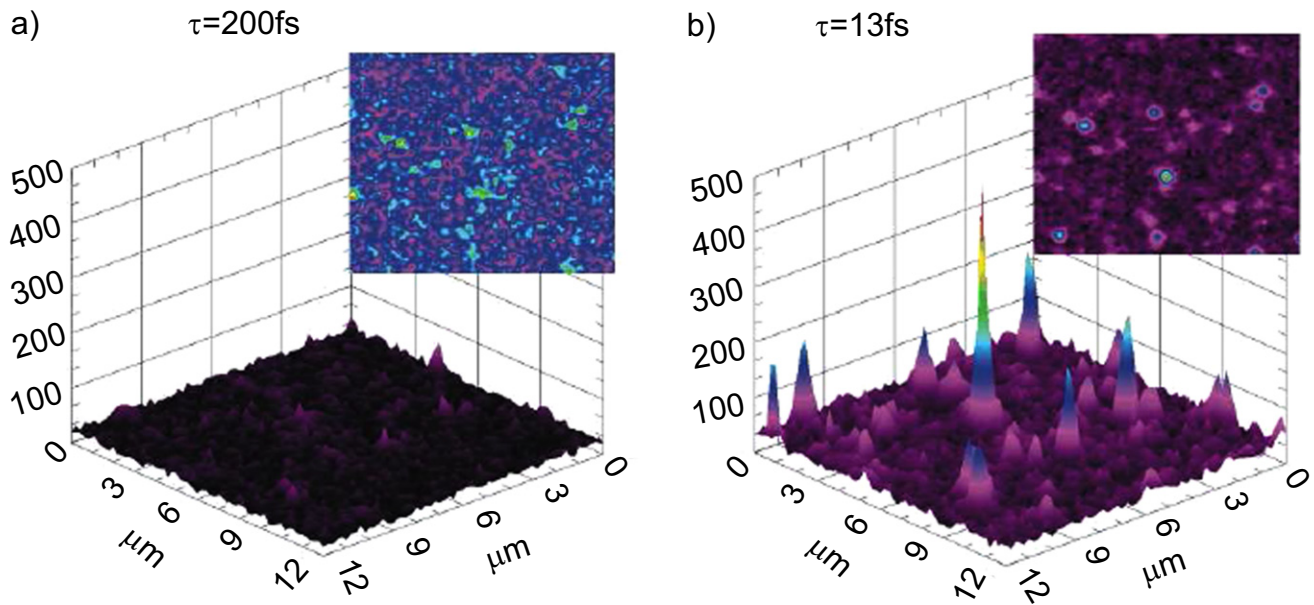
Figure 8. *Spectral phase sensitivity.* Images of individual KTP HNPs on a substrate obtained by 200 fs (a) and 13 fs (b) pulses. For each pulse duration both a three-dimensional graph of the SH intensity as well as a normalized two-dimensional map are shown. Reprinted (adapted) with permission from [65]. Copyright 2009 The Optical Society.

thickness L onto a HNP. The SH emission from the particle interferes with that of a reference beam and it is recorded on a CCD. The spatial phase information are then extracted by a algorithm and their complex conjugate is stored as a two-dimensional phase-mask on a light modulator (SLM). In a second step, a beam at 2ω is modified in phase by the SLM and focused through the same scattering medium. Thanks to the phase pre-correction the focus inside the scattering medium at the HNP location results quasi diffraction limited. For actually taking advantage of the correction for imaging, a rotation θ is applied on the beam. Such rotation displaces by $\Delta x = L\theta$ the focus with respect to its original position. As the speckle intensity correlation is proportional to $\left[\left(\frac{2\theta\pi L}{\lambda} \right) \middle/ \left(\sinh \left(\frac{2\theta\pi L}{\lambda} \right) \right) \right]^2$, the memory effect of the phase cumulated by scattering is limited to rotation $\theta < (\lambda/2\pi L)$. This values defines the extension of the visibility-corrected region in the focal plane [96]. A similar argument can be applied to the axial displacement Δz. The biggest advantage of phase conjugation is related to the fact that a single measurement of the two-dimensional speckle field allows setting-up the correction phase mask for a small volume around the HNP, while its main drawback is related to the necessity of a very precise alignment of the sample with respect to the beam. On the other hand, optimal wavefront and temporal shaping technique, relying on open- and close-loop iterative optimization procedures, although often slow, have the advantage of imposing less experimental constraints in terms of sample manipulation [97]. In 2011, three papers concerning the focusing and temporal compression of femtosecond pulses propagating through scattering media have almost simultaneously appeared [98–100]. In a wide sense, these researches pursued previous works by the Fink group at

ParisTech and Mosk group in Twente, by extending to broad bandwidth femtosecond pulses the results on spatial-phase compensation obtained for monochromatic CW lasers. These studies demonstrate how both spatial and temporal degrees of freedom can be manipulated to obtain well focused and temporally short femtosecond pulses at a given location after a scattering layer. According to the results of Accanto [92] and Extermann [56] presented here, HNPs could be excellent *in situ* probes thanks to their photo-stability and nonlinear sensitivity to intensity variations.

7. Conclusions

We have presented a comprehensive review of research studies on HNPs (i.e. noncentrosymmetric metal oxide nanoparticles with large $\chi^{(2)}$ response) with the aim of disseminating these results to the optical community. Introduced less than ten years ago as probes for multi-photon imaging, HNPs have attracted particular attention in the field of biological and medical sciences, however their features including coherent and polarization sensitive response, long term photo-stability, and spectral excitation tunability could be further exploited in other research contexts. One recent advancement particularly promising is the simultaneous and efficient generation of multi-harmonic orders by HNPs. This finding can be easily exploited in combination with new infrared ultrafast sources, enabling the detection of second and TH in the visible and UV-visible range, respectively. The approach can greatly benefit signal selectivity for bioimaging and detection [61, 70] but also opens previously unforeseen applications in other fields [68].

Acknowledgments

References

[1] Denk W, Strickler J H and Webb W W 1990 *Science* **248** 73–76
[2] Horton N G, Wang K, Kobat D, Clark C G, Wise F W, Schaffer C B and Xu C 2013 *Nat. Photonics* **7** 205–9
[3] Extermann J, Bonacina L, Cuna E, Kasparian C, Mugnier Y, Feurer T and Wolf J P 2009 *Opt. Express* **17** 15342–9
[4] Andresen V, Alexander S, Heupel W M, Hirschberg M, Hoffman R M and Friedl P 2009 *Curr. Opin. Biotechnol.* **20** 54–62
[5] Sargent E H 2005 *Adv. Mater.* **17** 515–22
[6] Boyd R W 2003 *Nonlinear Optics* (New York: Academic)
[7] Le Floc'h V, Brasselet S, Roch J F and Zyss J 2003 *J. Phys. Chem.* B **107** 12403–10
[8] Dempsey W P, Fraser S E and Pantazis P 2012 *Bioessays* **34** 351–60
[9] Bonacina L 2013 *Mol. Pharmaceutics* **10** 783–92
[10] Ladj R, Bitar A, Eissa M, Mugnier Y, Le Dantec R, Fessi H and Elaissari A 2013 *J. Mater. Chem.* B **1** 1381–96
[11] Butet J, Russier-Antoine I, Jonin C, Lascoux N, Benichou E and Brevet P F 2012 *J. Opt. Soc. Am.* B **29** 2213–21
[12] Winter S, Zielinski M, Chauvat D, Zyss J and Oron D 2011 *J. Phys. Chem.* C **115** 4558–63
[13] Zielinski M, Winter S, Kolkowski R, Nogues C, Oron D, Zyss J and Chauvat D 2011 *Opt. Express* **19** 6657–70
[14] Shaviv E and Banin U 2010 *ACS Nano* **4** 1529–38
[15] Golovan L and Timoshenko V Y 2013 *J. Nanoelectron. Optoelectron.* **8** 223–39
[16] Snaith H J 2013 *J. Phys. Chem. Lett.* **4** 3623–30
[17] Niederberger M, Pinna N, Polleux J and Antonietti M 2004 *Angew. Chem., Int. Ed.* **43** 2270–3
[18] Baruah S and Dutta J 2009 *Sci. Technol. Adv. Mater.* **10** 013001
[19] Adireddy S, Lin C, Cao B, Zhou W and Caruntu G 2010 *Chem. Mater.* **22** 1946–8
[20] Modeshia D R and Walton R I 2010 *Chem. Soc. Rev.* **39** 4303–25
[21] Nakayama Y, Pauzauskie P J, Radenovic A, Onorato R M, Saykally R J, Liphardt J and Yang P D 2007 *Nature* **447** 1098–U8
[22] Mohanty D, Chaubey G S, Yourdkhani A, Adireddy S, Caruntu G and Wiley J B 2012 *RSC Adv.* **2** 1913–6
[23] Aufray M, Menuel S, Fort Y, Eschbach J, Rouxel D and Vincent B 2009 *J. Nanosci. Nanotechnol.* **9** 4780–5
[24] Wang Y, Zhou X, Chen Z, Cai B, Ye Z, Gao C and Huang J 2014 *Appl. Phys.* A **117** 2121–6
[25] Le Xuan L, Zhou C, Slablab A, Chauvat D, Tard C, Perruchas S, Gacoin T, Villeval P and Roch J F 2008 *Small* **4** 1332–6
[26] Biswas S K, Pathak A and Pramanik P 2007 *J. Am. Ceram. Soc.* **90** 1071–6
[27] Mayer L, Slablab A, Dantelle G, Jacques V, Lepagnol-Bestel A M, Perruchas S, Spinicelli P, Thomas A, Chauvat D and Simonneau M 2013 *Nanoscale* **5** 8466–71

[28] Mayer L, Dantelle G, Jacques V, Perruchas S, Patriarche G, Roch J F and Gacoin T 2014 *J. Mater. Chem.* C **2** 7681–6
[29] Ladj R, Eissa M M, Valour J P, Mugnier Y, Le Dantec R, Fessi H, Dubled M, Galez C and Elaissari A 2014 *Sci. Adv. Mater.* **6** 102–10
[30] Mugnier Y *et al* 2011 *J. Phys. Chem.* C **115** 23–30
[31] Ladj R, El Kass M, Mugnier Y, Le Dantec R, Fessi H, Galez C and Elaissari A 2012 *Cryst. Growth Des.* **12** 5387–95
[32] Selbach S M, Einarsrud M, Tybell T and Grande T 2007 *J. Am. Ceram. Soc.* **90** 3430–4
[33] Zhu X, Hang Q, Xing Z, Yang Y, Zhu J, Liu Z, Ming N, Zhou P, Song Y and Li Z 2011 *J. Am. Ceram. Soc.* **94** 2688–93
[34] Schwung S, Rogov A, Clarke G, Joulaud C, Magouroux T, Staedler D, Passemard S, Justel T, Badie L and Galez C 2014 *J. Appl. Phys.* **116** 114306
[35] Shabani J, Mirkazemi S, Masoudpanah S and Abadi P T D 2014 *J. Supercond. Novel Magn.* **6** 2542–9
[36] Bardhan R, Lal S, Joshi A and Halas N J 2011 *Acc. Chem. Res.* **44** 936–46
[37] Staedler D *et al* 2012 *ACS Nano* **6** 2542–9
[38] Le Dantec R *et al* 2011 *J. Phys. Chem.* C **115** 15140–6
[39] O'Brien S, Brus L and Murray C B 2001 *J. Am. Chem. Soc.* **123** 12085–6
[40] Polking M J, Han M G, Yourdkhani A, Petkov V, Kisielowski C F, Volkov V V, Zhu Y, Caruntu G, Alivisatos A P and Ramesh R 2012 *Nat. Mater.* **11** 700–9
[41] Knabe B, Buse K, Assenmacher W and Mader W 2012 *Phys. Rev.* B **86** 195428
[42] Hsieh C L, Grange R, Pu Y and Psaltis D 2009 *Opt. Express* **17** 2880–91
[43] Culić-Viskota J, Dempsey W P, Fraser S E and Pantazis P 2012 *Nat. Protocols* **7** 1618–33
[44] Staedler D *et al* 2014 *Nanomed.: Nanotechnol. Biol. Med.* at press
[45] Kim E, Steinbruck A, Buscaglia M T, Buscaglia V, Pertsch T and Grange R 2013 *ACS Nano* **7** 5343–9
[46] Hsieh C L, Grange R, Pu Y and Psaltis D 2010 *Opt. Express* **18** 3456–7
[47] Williams R M, Zipfel W R and Webb W W 2005 *Biophys. J.* **88** 1377–86
[48] Clays K and Persoons A 1991 *Phys. Rev. Lett.* **66** 2980
[49] Roke S and Gonella G 2012 *Annu. Rev. Phys. Chem.* **63** 353–78
[50] Joulaud C, Mugnier Y, Djanta G, Dubled M, Marty J C, Galez C, Wolf J P, Bonacina L and Le Dantec R 2013 *J. Nanobiotechnol.* **11**
[51] Filipe V, Hawe A and Jiskoot W 2010 *Pharmaceutical Res.* **27** 796–810
[52] Kuzyk M G and Dirk C W 1998 *Characterization Techniques and Tabulations for Organic Non Linear Optical Materials* (New York: Dekker)
[53] Magouroux T, Extermann J, Hoffmann P, Mugnier Y, Le Dantec R, Jaconi M E, Kasparian C, Ciepielewski D, Bonacina L and Wolf J P 2012 *Small* **8** 2752–6
[54] Macias-Romero C, Didier M E P, Zubkovs V, Delannoy L, Dutto F, Radenovic A and Roke S 2014 *Nano Lett.*
[55] Li H F, Edwards P S, Zhang Z, Zhang B G, Xu Y, Gopalan V and Liu Z W 2011 *J. Opt. Soc. Am.* B **28** 2844–7
[56] Extermann J, Bonacina L, Courvoisier F, Kiselev D, Mugnier Y, le Dantec R, Galez C and Wolf J P 2008 *Opt. Express* **16** 10405–11
[57] Pu Y, Grange R, Hsieh C L and Psaltis D 2010 *Phys. Rev. Lett.* **104**
[58] Richter J, Steinbrück A, Pertsch T, Tünnermann A and Grange R 2012 *Plasmonics* **8** 115–20
[59] Richter J, Steinbrück A, Zilk M, Sergeyev A, Pertsch T, Tünnermann A and Grange R 2014 *Nanoscale* **6** 5200–7

[60] Extermann J, Bejot P, Bonacina L, Mugnier Y, Le Dantec R, Mazingue T, Galez C and Wolf J P 2009 *Appl. Phys. B* **97** 537–40

[61] Geissbuehler M, Bonacina L, Shcheslavskiy V, Bocchio N L, Geissbuehler S, Leutenegger M, Marki I, Wolf J P and Lasser T 2012 *Nano Lett.* **12** 1668–72

[62] Staedler D, Magouroux T, Passemard S, Schwung S, Dubled M, Schneiter G S, Rytz D, Gerber-Lemaire S, Bonacina L and Wolf J P 2014 *Nanoscale* **6** 2929–36

[63] Pantazis P, Maloney J, Wu D and Fraser S E 2010 *Proc. Natl Acad. Sci. USA* **107** 14535–40

[64] Kachynski A V, Kuzmin A N, Nyk M, Roy I and Prasad P N 2008 *J. Phys. Chem. C* **112** 10721–4

[65] Wnuk P, Le Xuan L, Slablab A, Tard C, Perruchas S, Gacoin T, Roch J F, Chauvat D and Radzewicz C 2009 *Opt. Exp.* **17** 4652–8

[66] Morita R and Yamashita M 1993 *Japan. J. Appl. Phys. 2* **32** 905–7

[67] Cai F, Yu J, Qian J, Wang Y, Chen Z, Huang J, Ye Z and He S 2014 *Laser Photonics Rev.* **8** 865–74

[68] Dai J, Yuan M H, Zeng J H, Dai Q F, Lan S, Xiao C and Tie S L 2014 *Appl. Opt.* **53** 189–94

[69] Débarre D, Supatto W, Pena A M, Fabre A, Tordjmann T, Combettes L, Schanne-Klein M C and Beaurepaire E 2005 *Nat. Methods* **3** 47–53

[70] Rogov A, Irondelle M, Ramos-Gomes F, Bode J, Staedler D, Passemard S, Courvoisier S, Yamamoto Y, Waharte F and Ciepielewski D 2014 arXiv:1410.7969

[71] Brasselet S, Le Floc'h V, Treussart F, Roch J F, Zyss J, Botzung-Appert E and Ibanez A 2004 *Phys. Rev. Lett.* **92** 207401

[72] Bonacina L, Mugnier Y, Courvoisier F, le Dantec R, Extermann J, Lambert Y, Boutou V, Galez C and Wolf J P 2007 *Appl. Phys. B* **87** 399–403

[73] Extermann J 2010 Nonlinear bio-imaging and detection with ultrafast lasers *PhD Thesis* Université de Genève, Faculté des Sciences

[74] Sandeau N, Le Xuan L, Chauvat D, Zhou C, Roch J F and Brasselet S 2007 *Opt. Express* **15** 16051–60

[75] Grange R, Choi J W, Hsieh C L, Pu Y, Magrez A, Smajda R, Forro L and Psaltis D 2009 *Appl. Phys. Lett.* **95** 143105

[76] Hsieh C L, Pu Y, Grange R and Psaltis D 2010 *Opt. Express* **18** 11917–32

[77] Munhoz F, Gasecka A, Brustlein S and Brasselet S 2008 *Opt. Express* **16** 20891–901

[78] van der Veen M A, Vermoortele F, De Vos D E and Verbiest T 2012 *Anal. Chem.* **84** 6378–85

[79] van der Veen M A, Vermoortele F, De Vos D E and Verbiest T 2012 *Anal. Chem.* **84** 6386–90

[80] Naskali L, Huttunen M J, Virkki M, Bautista G, Dér A and Kauranen M 2014 *J. Phys. Chem. C* **118** 26409–14

[81] Paskover Y, Xie D, Laforge F O and Rabitz H 2014 *J. Opt. Soc. Am. B* **31** 1165–73

[82] Baumner R, Bonacina L, Enderlein J, Extermann J, Fricke-Begemann T, Marowsky G and Wolf J P 2010 *Opt. Express* **18** 23218–25

[83] Enderlein J 2000 *Opt. Lett.* **25** 634–6

[84] Böhmer M and Enderlein J 2003 *J. Opt. Soc. Am. B* **20** 554–9

[85] Gachet D, Sandeau N and Rigneault H 2006 Far-field radiation pattern in coherent anti-stokes raman scattering (cars) microscopy *Biomedical Optics (Int. Society for Optics and Photonics)* 609309

[86] Amat-Roldán I, Cormack I G, Loza-Alvarez P and Artigas D 2004 *Opt. Lett.* **29** 2282–4

[87] Trebino R 2000 *Frequency-Resolved Optical Gating: The Measurement of Ultrashort Laser Pulses: The Measurement of Ultrashort Laser Pulses* vol 1 (Berlin: Springer)

[88] Li H F, Zhang Z, Xu Q A, Shi K B, Jia Y S, Zhang B G, Xu Y and Liu Z W 2010 *Appl. Phys. Lett.* **97** 261108

[89] Li H F, Jia Y S, Xu Q, Shi K B, Wu J, Eklund P C, Xu Y and Liu Z W 2010 *Appl. Phys. Lett.* **96** 021103

[90] Mehta N, Yang C, Xu Y and Liu Z 2014 *Opt. Express* **22** 11099–106

[91] Muller M, Squier J, Wolleschensky R, Simon U and Brakenhoff G J 1998 *J. Microsc.* **191** 141–50

[92] Accanto N, Nieder J B, Piatkowski L, Castro-Lopez M, Pastorelli F, Brinks D and van Hulst N F 2014 *Light: Sci. Appl.* **3** e143

[93] Lozovoy V V, Pastirk I and Dantus M 2004 *Opt. Lett.* **29** 775–7

[94] Le Xuan L, Brasselet S, Treussart F, Roch J F, Marquier F, Chauvat D, Perruchas S, Tard C and Gacoin T 2006 *Appl. Phys. Lett.* **89** 121118

[95] Pu Y, Centurion M and Psaltis D 2008 *Appl. Opt.* **47** 103–10

[96] Feng S, Kane C, Lee P A and Stone A D 1988 *Phys. Rev. Lett.* **61** 834

[97] Booth M J 2007 *Phil. Trans. R. Soc. A* **365** 2829–43

[98] Katz O, Small E, Bromberg Y and Silberberg Y 2011 *Nat. Photonics* **5** 372–7

[99] Mosk A P, Lagendijk A, Lerosey G and Fink M 2012 *Nat. Photonics* **6** 283–92

[100] McCabe D J, Tajalli A, Austin D R, Bondareff P, Walmsley I A, Gigan S and Chatel B 2011 *Nat. Commun.* **2** 447